Since January 2020 Elsevier has created a COVID-19 resource centre with free information in English and Mandarin on the novel coronavirus COVID-19. The COVID-19 resource centre is hosted on Elsevier Connect, the company's public news and information website.

Journal of Molecular Structure 1265 (2022) 133391

Contents lists available at ScienceDirect

Journal of Molecular Structure

journal homepage: www.elsevier.com/locate/molstr

Synthesis, crystal structure, and a molecular modeling approach to identify effective antiviral hydrazide derivative against the main protease of SARS-CoV-2

Shaaban K. Mohamed[a,b], Youness El Bakri[c,*], Dalia A. Abdul[d], Sajjad Ahmad[e], Mustafa R Albayati[f], Chin-Hung Lai[g,h], Joel T. Mague[i], Mahmoud S. Tolba[j]

[a] Chemistry and Environmental Division, Manchester Metropolitan University, Manchester M1 5GD, United Kingdom
[b] Chemistry Department, Faculty of Science, Minia University, 61519 El-Minia, Egypt
[c] Department of Theoretical and Applied Chemistry, South Ural State University, Lenin prospect 76, Chelyabinsk 454080, Russia
[d] Department of Chemistry, College of Science, university of Sulaimani, Sulaimania, Iraq
[e] Department of Health and Biological Sciences, Abasyn University, Peshawar 25000, Pakistan
[f] Kirkuk University, College of Science, Department of Chemistry, Kirkuk, Iraq
[g] Department of Medical Applied Chemistry, Chung Shan Medical University, Taichung 40241, Taiwan
[h] Department of Medical Education, Chung Shan Medical University Hospital, 402 Taichung, Taiwan
[i] Department of Chemistry, Tulane University, New Orleans, LA 70118, United States
[j] Chemistry Department, Faculty of Science, New Valley University, El-Kharja 72511, Egypt

ARTICLE INFO

Article history:
Received 26 November 2021
Revised 22 May 2022
Accepted 27 May 2022
Available online 28 May 2022

Keywords:
SARS-CoV-2
Hydrazide
Crystal structurey
DFT calculations
Molecular docking
Molecular dynamics simulations

ABSTRACT

In the fall of 2019, a new type of coronavirus took place in Wuhan city, China, and rapidly spread across the world and urges the scientific community to develop antiviral therapeutic agents. In our effort we have synthesized a new hydrazide derivative, (*E*)-*N*'-(1-(4-bromophenyl)ethylidene)-2-(6-methoxynaphthalen-2-yl)propanehydrazide for this purpose because of its potential inhibitory proprieties. The asymmetric unit of the title molecule consists of two independent molecules differing noticeably in conformation. In the crystal, the independent molecules are linked by N—H···O and C—H···O hydrogen bonds and C—H···π(ring) interactions into helical chains extending along the b-axis direction. The chains are further joined by additional C—H···π(ring) interactions into the full 3-D structure. To obtain a structure-activity relationship, the DFT-NBO analysis is performed to study the intrinsic electronic properties of the title compound. Molecular modeling studies were also conducted to examine the binding affinity of the compound for the SARS-CoV-2 main protease enzyme and to determine intermolecular binding interactions. The compound revealed a stable binding mode at the enzyme active pocket with a binding energy value of -8.1 kcal/mol. Further, stable dynamics were revealed for the enzyme-compound complex and reported highly favorable binding energies. The net MMGBSA binding energy of the complex is -37.41 kcal/mol while the net MMPBSA binding energy is -40.5 kcal/mol. Overall, the compound disclosed the strongest bond of ing the main protease enzyme and might be a good lead for further structural optimization.

1. Introduction

There is no doubt that there are many organic compounds with good biological and pharmacological activities confirming the importance of organic compounds in different fields [1–3]. Non-steroidal anti-inflammatory drugs (NSAIDs) are one of the largest medicinal applicable drugs as an analgesic, antipyretic, anti-inflammatory, and anti-viral agents [4].

The S-enantiomer Naproxen, 2-(6-methoxynaphthalen-2-yl)propionic acid, is one of the most regularly used propionic acid derivatives for the treatment of various diseases such as anti-inflammatory effects [5]. Anti-inflammatory effects of naproxen and its derivatives are generally thought to be related to its inhibition of COX and consequent decrease in prostaglandin concentrations in various fluids and tissues [6]. It was also reported that naproxen amide derivatives showed good antibacterial activity against Gram-positive bacteria such as Staphylococcus aureus and

* Corresponding author at: Chemistry, Chelyabinsk State Technical University: Uzno-Ural'skij gosudarstvennyj universitet, Laboratoire de Chimie Organique Hét, MA, 10014 Rabat, Russia.
E-mail address: yns.elbakri@gmail.com (Y. El Bakri).

https://doi.org/10.1016/j.molstruc.2022.133391
0022-2860/

Bacillus subtilis and Gram-negative back such eria as Escherichia coli and Pseudomonas aeruginosa comparable to standard drugs Ampicillin and Ciprofloxacin [7]. Meanwhile, naproxen itself was tested in vitro for the inhibition of four kinds of human cancer cells, KB, A-549, MDA, and Bell-7402. The data showed that the inhibition rate of naproxen on KB cells was higher than that of 5-fluorouracil due to their intercalating effect on DNA [8].

On the other hand, fears have been raised that non-steroidal anti-inflammatory drugs could be accompanied by a risk for adverse effects when they are used in patients with acute viral respiratory infections, including COVID-19 [9,10]. One of these opinions against the use of NSAIDs and acetaminophen is that these medications are antipyretic drugs that could hide a rising fever accompanied by COVID-19 and thus delay diagnosis and fast spread of the infection [11]. However, there is no strong evidence against or with the use of NSAIDs in patients diagnosed with COVID-19. Moreover, even if evidence was found favoring or rejecting one particular NSAID in this setting, it is not clear whether such evidence could apply to all NSAIDs similarly [12]. Theoretically, NSAIDs when used in the early stages during the clinical course of COVID-19 might control disease development or even reverse lymphocytopenia [13].

Naproxen is a non-steroidal anti-inflammatory drug that has previously been shown to exert antiviral activity against the influenza A virus by inhibiting nucleoprotein (NP) binding to RNA. Naproxen is a potential broad, multi-mechanistic anti-influenza virus therapeutic, as it inhibits influenza B virus replication both in vivo and in vitro. The anti-influenza B virus activity of Naproxen is more effective than that of the commonly used neuraminidase inhibitor oseltamivir in mice [14]. In the case of COVID-19, The NSAIDs Naproxen and indomethacin have both been found to have antiviral activity. Indomethacin was investigated in vitro and in animal patterns and found to have potential direct antiviral activity against SARS-CoV (severe acute respiratory syndrome coronavirus) and CCTV (canine coronavirus) via interference with viral RNA synthesis [15]. Animal patterns have shown that Naproxen also has antiviral activity against influenza A and B viruses by interfering with the RNA replication process [14,16]. As the COVID-19 virus is a single-stranded RNA virus, it was proposed that naproxen could be “the most probable agent for the management of widespread novel coronavirus infection” [17]. A study in BMJ mentioned the potential role of Naproxen in the protection and curing of COVID-19 patients in regions that have limited access to medications currently used in the world such as Iran [18]. Meanwhile, another published article has shown the increased ACE2 expression by ibuprofen administration, which may lead to an increased risk of COVID-19 infection in this country [19]. The most important issues which should be taken more attention to about the use of NSAIDs in acute Respiratory tract infections (RTIs)are the deterioration in the symptoms, the subsequent effects following the use of these medications, and the adverse cardiovascular effects which are classified as a risk factor in RTIs including COVID-19 [20,21]. However, the side effects are different among NSAIDs; Ibuprofen, Coxibs, and Diclofenac represent the highest cardiovascular complications while Naproxen (even with high doses) did not show any significant cardiovascular problems in a randomized clinical trial (RCTs) [22]. To date, there is no sufficient available evidence to evaluate the safety and efficiency of NSAIDs with COVID-19. But, if the patients’ symptoms are not reduced by acetaminophen, the first choice among NSAIDs Could be Naproxen (because of the less cardiovascular side effects and more evidence for its effectiveness in influenza) and the second choice may be indomethacin (according to available in vitro and in vivo evidence for SARS) [23].

Based on these facts, signals, and points and further to our efforts toward modification and manipulation of NSAIDs especially Naproxen, we report the synthesis of the new suggested Naproxen-based hydrazone as an agent to control COVID-19.

Molecular modeling studies such as molecular docking and molecular dynamics simulations are now applied commonly to decipher the synthesized compound binding with the SARS-CoV-2 main protease enzyme. The binding stability of the compound with ith enzyme was further evaluated by MMGBSA and MMPBSA binding energy methods.

2. Materials and methods

2.1. Synthesis of (E)-N’-(1-(4-bromophenyl)ethylidene)-2-(6-methoxynaphthalen-2-yl)propanehydrazide (4)

In 100 mL RBF, 25 mL of ethanol was added to a mixture of 1mmol of 4-bromoacetophenone (199 mg) and 1mmol of Naproxen acid hydrazide (244 mg). The reaction mixture was refluxed for 6 h and monitored by TLC until completion. The crude solid was obtained and recrystallized from ethanol to afford a colorless crystal suitable for X-ray diffraction with m.p = 164-166 °C (Scheme 1).

IR (KBr): (C=O amide 1666 cm^{-1}), (NH 3234 cm^{-1}), (-C=N 1606 cm^{-1}). ^{1}H NMR (400MHz, DMSO): δ = 1.4 (d, 3H, CH_3), 3.5 (q, 1H, C-H), 3.8 (s, 3H, OCH_3),2.3(s,3H, CH_3), 10.5 (s, 1H, -NH), 7.0- 7.7 (m, 10H, aromatic protons) .^{13}C-NMR δ=15(CH3),16(CH3), 45 (C-H aliphatic), 55 (OCH_3), 105-156 (16 aromatic carbons), 148 (C=N), 175 (C=O amide). Massspectra were obtained in Varian MAT 311 doubly focusinginstrument using electron impact ionization (70 eV); ESI-MS: (M) m/z= 424.00, mono-isotop (M^{+2}) = 426.00. Elemental analyses were carried out at MicroanalyticalCenter, Cairo University, Egypt. Anal. calcd (%) for $C_{22}H_{21}BrN_2O_2$; C: 62.13, H: 4.98, N: 6.59 found: C: 62.15, H: 5:00, N: 6.60.

2.2. X-ray structure determination

A suitable crystal of 4 was mounted on a polymer loop with a drop of heavy oil and placed in a cold nitrogen stream on a Bruker D8 Quest diffractometer equipped with a PHOTON 3 detector. The diffraction data were obtained from 11 sets of frames, each of width 0.5° in ω or φ, collected with scan parameters determined by the "strategy" routine in *APEX3* [24] and using Mo Kα (λ = 0.71074 Å) radiation. The scan time was 20 sec/frame. The raw intensity data were converted to F^2 values by *SAINT* and correction for absorption and merging of equivalent reflections was performed with *SADABS* [25]. The structure was solved by dual space methods (*SHELXT* [26]) and refined by full-matrix, least-squares procedures (*SHELXT* [27]). Hydrogen atoms attached to carbon were included as riding contributions in idealized positions with isotropic displacement parameters tied to those of the attached atoms. Those attached to nitrogen were refined with restraints that the N–H distances approximate ideal values. Five reflections affected by the beam stop were omitted from the final refinement. The final difference map was essentially featureless.

The details concerning collections and analyses are described in Table 1.

2.3. The Hirshfeld surface analysis and Energy framework

Both the definition of a molecule in a condensed phase and the recognition of distinct entities in molecular liquids and crystals are fundamental concepts in chemistry. Based on Hirshfeld’s partitioning scheme, Spackman et al. 1997 proposed a method to divide the electron distribution in a crystalline phase into molecular fragments [28–30]. Their proposed method partitioned the crystal into regions where the electron distribution of a sum of spherical atoms

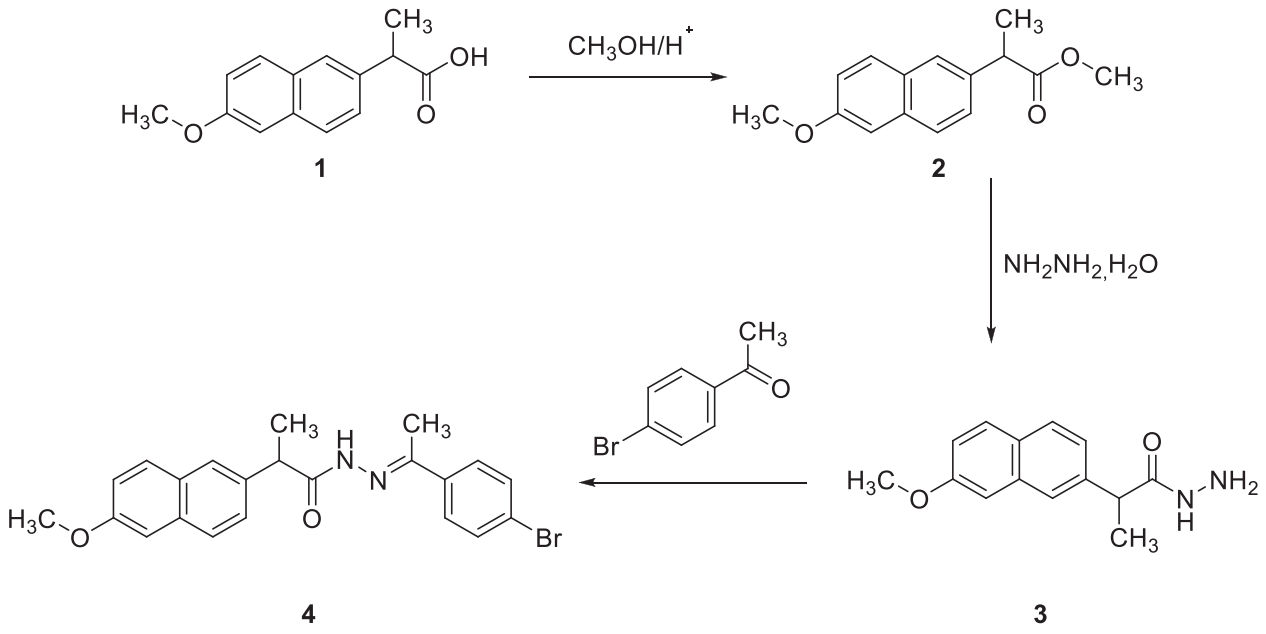

Scheme 1. The synthesis route of 4.

Table 1
Crystal data and structure refinement details for compound 4.

Chemical formula	$C_{22}H_{21}BrN_2O_2$
CCDC Number	2122824
M_r	425.32
Crystal system, space group	Monoclinic, $P2_1$
Temperature (K)	150
a, *b*, *c* (Å)	10.5223 (5), 14.1944 (6), 13.5465 (6)
β (°)	104.081 (2)
V (Å^3)	1962.48 (15)
Z	4
Radiation type	Mo *Kα*
μ (mm$^{-1)}$	2.11
Crystal size (mm)	0.35 × 0.21 × 0.05
Data collection	
Diffractometer	Bruker D8 QUEST PHOTON 3 diffractometer
Absorption correction	Numerical *SADABS* (Krause et al., 2015)
T_{min}, T_{max}	0.70, 0.91
No. of measured, independent and observed [I > 2σ(I)] reflections	105687, 10596, 9565
R_{int}	0.033
(sin $\theta/\lambda)_{max}$ (Å^{-1})	0.687
Refinement	
$R[F^2 > 2\sigma(F^2)]$, $wR(F^2)$, *S*	0.028, 0.068, 1.04
No. of reflections	10596
No. of parameters	501
No. of restraints	3
H-atom treatment	H atoms are treated by a mixture of independent and constrained refinement
$\Delta\rho_{max}$, $\Delta\rho_{min}$ (e Å^{-3})	0.51, −0.30
Absolute structure	Flack x determined using 4194 quotients [(I+)-(I-)]/[(I+)+(I-)] (Parsons *et al.*, 2013).
Absolute structure parameter	0.0111 (17)

for the molecule dominates over the corresponding sum of the crystal. Because it is derived from Hirshfeld's stockholder partitioning, the molecular surface is named the Hirshfeld surface. Recently, the energy framework has been developed into a powerful tool that aids in better understanding crystal packing. Energy frameworks were constructed based on the energies (electrostatic, polarization, dispersion, and exchange-repulsion) calculated using the CE-B3LYP hybrid functional and 6-31G(d,p) basis set [31]. A cluster of radius 3.8 Å molecules was generated was considered around the central molecule and energy calculations were performed. The partition of the interaction energy (E_tot) can be represented as

$$E\_tot = k\_eleE\_ele + k\_polE\_pol + k\_disE\_dis + k\_repE\_rep \quad (1)$$

where ask represents the scale factor, E_ele= electrostatic component; E_pol= polarization energy, E_dis= dispersion energy and E_rep= exchange repulsion energy. In this study, both the Hirshfeld surface analysis and energy framework of the title compound were performed using the Crystal Explorer program [32].

2.4. The DFT and NBO studies

The structure in the gas phase of the title compound was optimized using density functional theory. The DFT calculation was performed by the hybrid B3LYP method, which is based on the idea of Becke and considers a mixture of the exact (HF) and DFT exchange utilizing the B3 functional, together with the LYP

correlation functional [33–35]. In conjunction with the basis set 6-311++G**, the B3LYP calculation was done [36]. After obtaining the converged geometry, the harmonic vibrational frequencies were calculated on the same theoretical level to confirm the number of imaginary frequencies is zero for the stationary point. To investigate the intrinsic electronic properties of the studied compounds, the NBO analysis of the survey compound was performed on the same theoretical level. All calculations of the title compound were done by the Gaussian 16 program [37].

2.5. The QTAIM study

To investigate the hydrogen bonding pattern in the title compound, the quantum theory of atoms in molecules (QTAIM) is also utilized by the Multiwfn program [38] in this study. According to QTAIM, if D-H forms a hydrogen bond with A, there should be a bond critical point (BCP) between H and A. In addition, criteria about the electron density (ρ_b) and the Laplacian of electron density ($\nabla^2\rho_b$) at BCPs have been established by Koch and Popelier to distinguish hydrogen bonding from van der Waals interactions [39]. According to the criteria, to represent a hydrogen bond that exists between D-H and A, the BCP between H and A should have aanelectron density in the range 0.002 - 0.034 a.u., and a Laplacian of electron density in the range 0.024 - 0.139 a.u.

2.6. Molecular Modeling Studies

The binding affinity of the synthesized compound for the SARS-CoV-2 main protease enzyme was deciphered through the molecular docking technique [40]. For this, the enzyme crystal structure was retrieved from the protein data bank (PDB ID: 7BQY). The structure was imported to UCSF Chimera 1.15 [41] where all associated ligands were removed including irrelevant water molecules and co-crystallized N3 ligand. The compound structure was drawn in ChemDraw 12.0 [42] and energy was minimized and converted into .pdb format. Molecular docking was carried out using AutoDock 4.2.6 [43]. Both the compound and protein were considered as inputs in the docking study. Polar hydrogen atoms were added. The grid box was set at the active pocket of the enzyme (Cys145). The box coordinates are: center_x = 6.00 Å, center_y = 4.87 Å, and center_z = 17.16 Å. The dimensions of the box is size_x = 25.0 Å, size_y = 25.0 Å and size_z = 25.0 Å. The number of conformations generated for the compound is 20 and the one with the lowest binding energy was considered as fittest conformation and complexed with the enzyme. The complex was then visualized for interactions and binding using USCF Chimera 1.15 [41] and Discovery studio v2021 [44].

2.7. Molecular dynamics simulation

Molecular dynamics simulation of the complex is done using an antechamber program of AMBER20 [45]. The topology of the complex is recorded using the LEAP module. The complex was then submerged into a TIP3P box and neutralized using 10 Na^+ ions. The complex was energy minimized via 750 steps of the steepest descent and 750 steps of conjugate gradient methods. Afterward, the system was heated gradually and heated for 50 ps at 300 K. This was followed by equilibration for 200 ps. The production run was performed for 100 ns using an explicit water model. During the process, the long-term interactions were modeled through the particle-mesh-Ewald method [46]. The hydrogen bonds were constrained using the SHAKE algorithm [47]. The simulation trajectories were investigated using the CPPTRAJ module [48] and different statistical plots were generated via XMGRACE [49].

Table 2
Hydrogen-bond geometry (Å) Cg1, Cg3, and Cg5 are, respectively, the centroids of the C1/C2/C3/C8/C9/C10, the C17·C22 and the C23/C24/C25/C30/C31/C32 rings.

D—H·A	*D*—H	H···A	*D*···A	*D*—H···A
N1—H1·O3[i]	0.905 (14)	1.986 (14)	2.889 (3)	175 (3)
N3—H3·O1[ii]	0.901 (13)	2.040 (15)	2.920 (3)	165 (3)
C21—H21·Cg5[iii]	0.95	2.97	3.576 (3)	123
C24—H24·Cg3	0.95	2.78	3.643 (3)	152
C33—H33C·Cg1[iv]	0.98	2.77	3.643 (3)	149
C38—H38A·O1[ii]	0.98	2.50	3.116 (3)	120

[i] −x+1, y+1/2, −z+1
[ii] −x+1, y−1/2, −z+1
[iii] −x, y+1/2, −z+1
[iv] −x, y−1/2, −zSymmetry codes

Further, intermolecular interaction energies were determined using the MMPBSA.py module of AMBER [50]. For this, 1000 frames were picked from the simulation and analyzed via MMPB/GBSA equation [51].

3. Results and discussion

3.1. Description of the crystal structure

The asymmetric unit consists of two independent molecules (M1 and M2; Fig. 1) which differ in conformation in several ways. The naphthyl groups are not planar with dihedral angles between the constituent planes of 2.11(5) and 4.32(12)° in M1 and M2 respectively. Most notably, the dihedral angle between the mean planes defined by C1/C2/C3/C8/C9/C10 and by O2/C14/N1/N2 is 50.09(11)° in M1 but the angle between the corresponding O3/C36/N3/N4 and C23/C24/C25/C30/C31/C32 planes in M2 is 79.96(17)°. Finally, the dihedral angle between the O2/C14/N1/N2 and C17···C22 mean planes in M1 is 50.85(8)° while that between the O3/C36/N3/N4 and C39···C44 mean planes in M2 is 26.50(18)°. The two independent molecules are connected by a C24—H24···Cg3 interaction (Table 2 and Fig. 1). In the crystal, N1—H1···O3, N3—H3···O1, and C38—H38A···O1 hydrogen bonds connect pairs of molecules which are then joined into helical chains extending along the b-axis direction by the C24—H24···Cg3 interactions (Table 2 and Fig. 2). These units are connected by C21—H21···Cg5 and C33—H33C···Cg1 interactions to form the final 3-D structure (Table 2 and Fig. 3).

3.2. The Hirshfeld analysis of the title compound

The standard resolution molecular Hirshfeld surface (d_{norm}) of the title compound was depicted in Fig. 4. The surface is shown as transparent so the molecular moiety can be visualized in a similar orientation for all of the structures around which they were calculated. The 3D d_{norm} surface can be used to identify very close intermolecular interactions. The value of d_{norm} is negative (positive) when intermolecular contacts are shorter (longer) than the van der Waals radii. The d_{norm} value is mapped onto the Hirshfeld surface with red, white, or blue colors. The red regions represent closer contacts with a negative d_{norm} value while the blue regions represent longer contacts with a positive d_{norm} value. Moreover, the white regions represent contacts equal to the van der Waals separation and have a d_{norm} value of zero. The previous studies about related nitrogenated species showed that they might have H···O, H···N, and H···Br hydrogen bonds [51–54]. In agreement with the previous studies, the d_{norm} Hirshfled surface of the title compound (Fig. 4(a) and 4(b)) showed there are H···O, H···N, and H···Br hydrogen bonds in the title compounds. Moreover, there is not either touching complementary pair of triangles in the shape index sur-

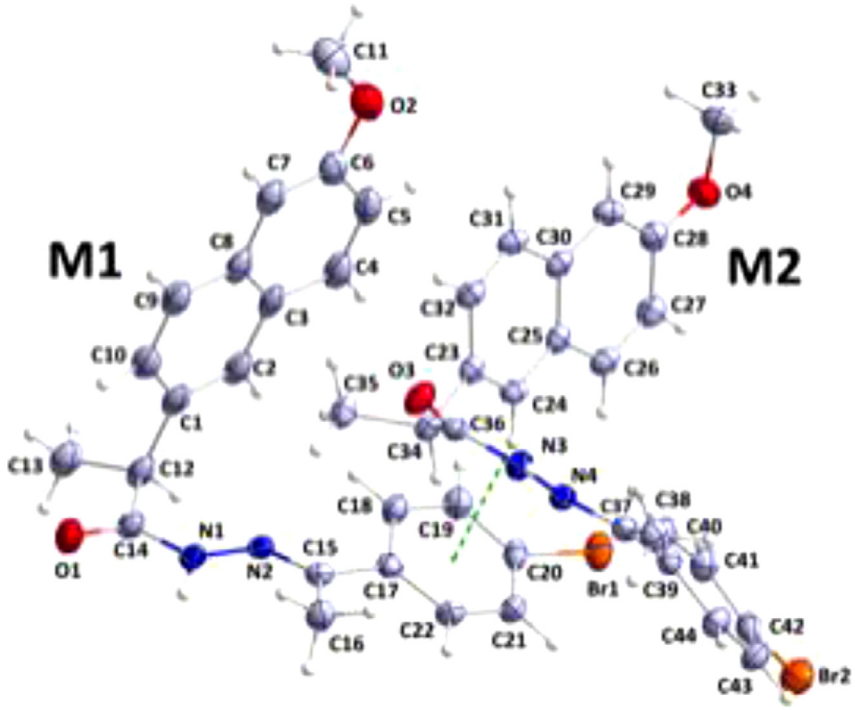

Fig. 1. The asymmetric unit with labeling scheme and 50% probability ellipsoids. The C—H···π(ring) interaction is depicted by a dashed line.

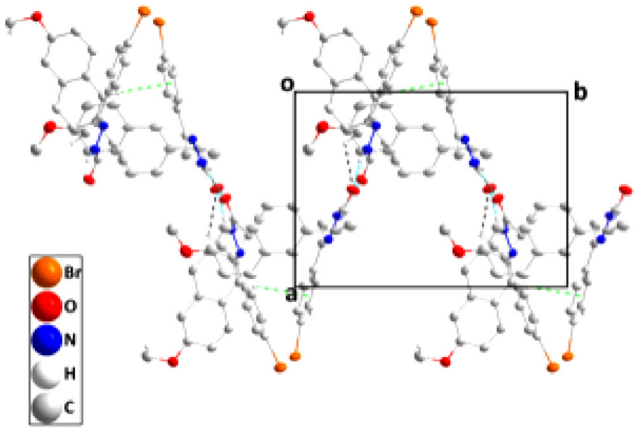

Fig. 2. A portion of one chain viewed along the c-axis direction with N—H···O and C—H···O hydrogen bonds depicted, respectively by light blue and black dashed lines. The C—H···π(ring) interactions are depicted by green dashed lines.

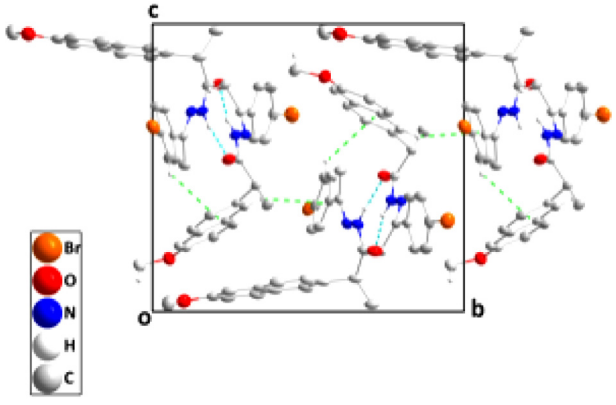

Fig. 3. Packing is viewed along the a-axis direction with intermolecular interactions depicted in Fig. 2.

face or large, green-colored, and flat regions in the curvedness surface (Fig. 4(c) and 4(d)), which indicates that relevant π-stacking interactions should be very weak in the crystal packing for the title compound, although the spot 5 in Fig. 4(a) or 4(b) might indicate a C···C contact. The results of the Hirshfeld surfaces are very similar to the related nitrogenated species in the previous study [52–54]. To understand the relative importance of these hydrogen bonds, we further performed an investigation of the 2D fingerprint plots of the title compound.

The 2D fingerprint plots highlight particular atom pair contacts and enable the separation of contributions from different interaction types that overlap in the full fingerprint. Using the standard 0.6 - 2.6 view with the de and di distance scales displayed on the graph axes and including the reciprocal contacts, we found the most important interaction involving hydrogen in the title compound was the H···H contact among all the studied compounds.

3.3. The Energy Framework

The energy framework of the titled compounds was summarized in Table 3, Table 4, and Fig. 5, Fig. 6. As listed in Table 3, and Fig. 6, the crystal packing for the title compound is mainly contributed by the dispersion interactions among molecules. It is in agreement with the previous studies about the related nitrogenated derivatives [52–55]. The previous studies about the related nitrogenated derivatives also showed that E_dis was the most important contributor to E_tot although the central molecule might form hydrogen bonds with its neighboring molecules.

3.4. The DFT studies of the title compounds

To rationalize the relationship between the intrinsic electronic properties and the chemical reactivities (biological activities) of the title compounds, a gas-phase DFT study was performed utilizing the B3LYP functional. The B3LYP-optimized geometry of the title compound was depicted in Fig. 7.

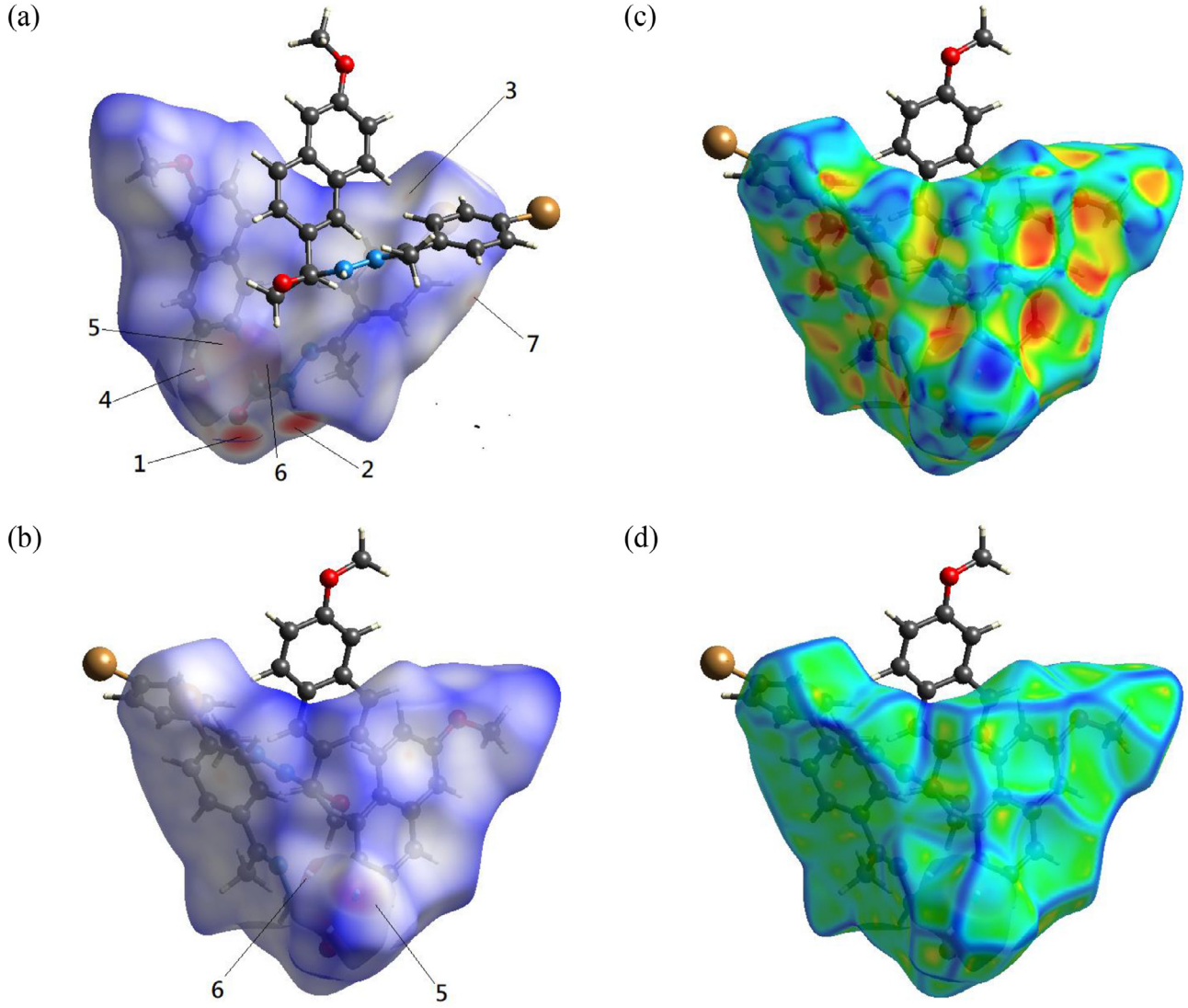

Fig. 4. The Hirshfeld surface (a) dnorm (red: negative, white: zero, blue: positive; scale: -0.5615~1.6157), (b) dnorm rotated by 180°, (c) shape index (scale: -1.0000~1.0000), (d) curvedness (scale: -4.0000~0.4000) of the title compound.

Table 3
The energy framework of the title compounds (energy in kJ/mol and R in Å).

N[a]	Symop	R[b]	Electron Density	E_ele	E_pol	E_dis	E_rep	E_tot
0	-x, y+1/2, -z	9.32	B3LYP/6-31G(d,p)	-1.9	-0.7	-19.4	6.8	-15.1
1	-	9.95	B3LYP/6-31G(d,p)	0.0	nan	0.0	0.0	nan
0	x, y, z	10.52	B3LYP/6-31G(d,p)	0.0	0.0	0.0	0.0	0.0
0	-	10.73	B3LYP/6-31G(d,p)	0.0	-0.0	-0.0	0.0	0.0
0	-	14.24	B3LYP/6-31G(d,p)	-0.0	-0.0	-0.0	0.0	-0.0
0	-	9.05	B3LYP/6-31G(d,p)	0.0	-0.0	-0.2	0.0	-0.2
0	-x, y+1/2, -z	11.48	B3LYP/6-31G(d,p)	0.0	-0.0	-0.0	0.0	0.0
0	-x, y+1/2, -z	7.26	B3LYP/6-31G(d,p)	0.0	-0.0	-0.0	0.0	0.0
0	-	5.35	B3LYP/6-31G(d,p)	-0.4	-0.1	-0.8	0.0	-1.2
0	-	5.66	B3LYP/6-31G(d,p)	-1.9	-0.7	-19.4	6.8	-15.1
0	-	10.61	B3LYP/6-31G(d,p)	-1.9	-0.7	-19.4	6.8	-15.1
0	x, y, z	10.52	B3LYP/6-31G(d,p)	-3.5	-0.9	-19.1	17.0	-10.5
0	-	14.02	B3LYP/6-31G(d,p)	-0.1	-0.0	-0.1	0.0	-0.2
0	-	10.82	B3LYP/6-31G(d,p)	-0.4	-0.7	-10.5	0.0	-10.2

[a] N refers to several molecules with R.
[b] R is the distance between molecular centroids (mean atomic position).

Table 4
The scale factor for CE-B3YLP model energies with B3LYP/6-31G(d,p) monomer electron densities.

Energy Model	k_ele	k_pol	k_disp	k_rep
CE-B3LYP ... B3LYP/6-31G(d,p) electron densities	1.057	0.740	0.871	0.618

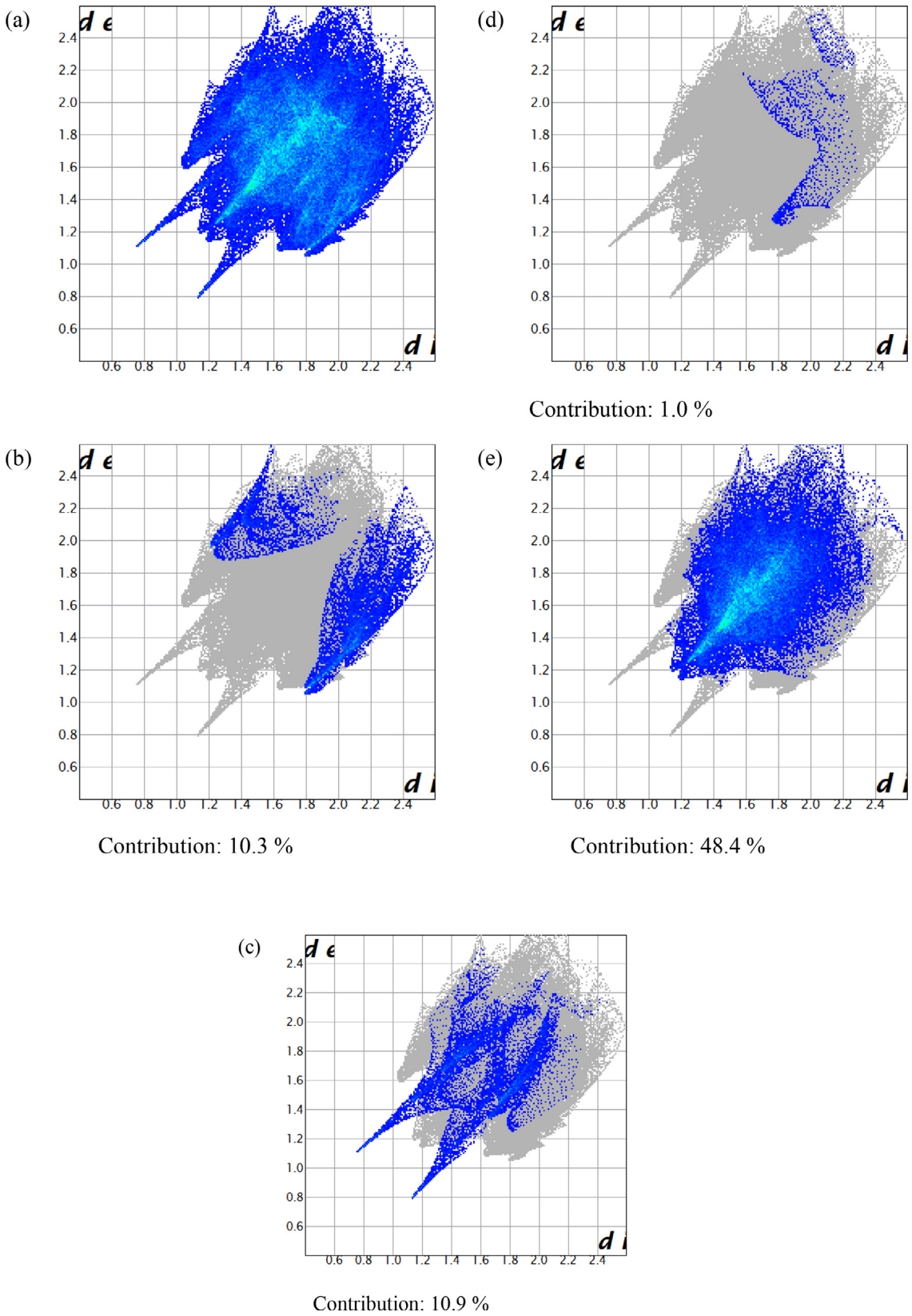

Fig. 5. The 2D fingerprint plot of the title compound is (a) full, (b) resolved by the H···Br contacts, (c) resolved by the H···O contacts, and (d) resolved by the H···N contacts, and (e) resolved by the H···H contacts.

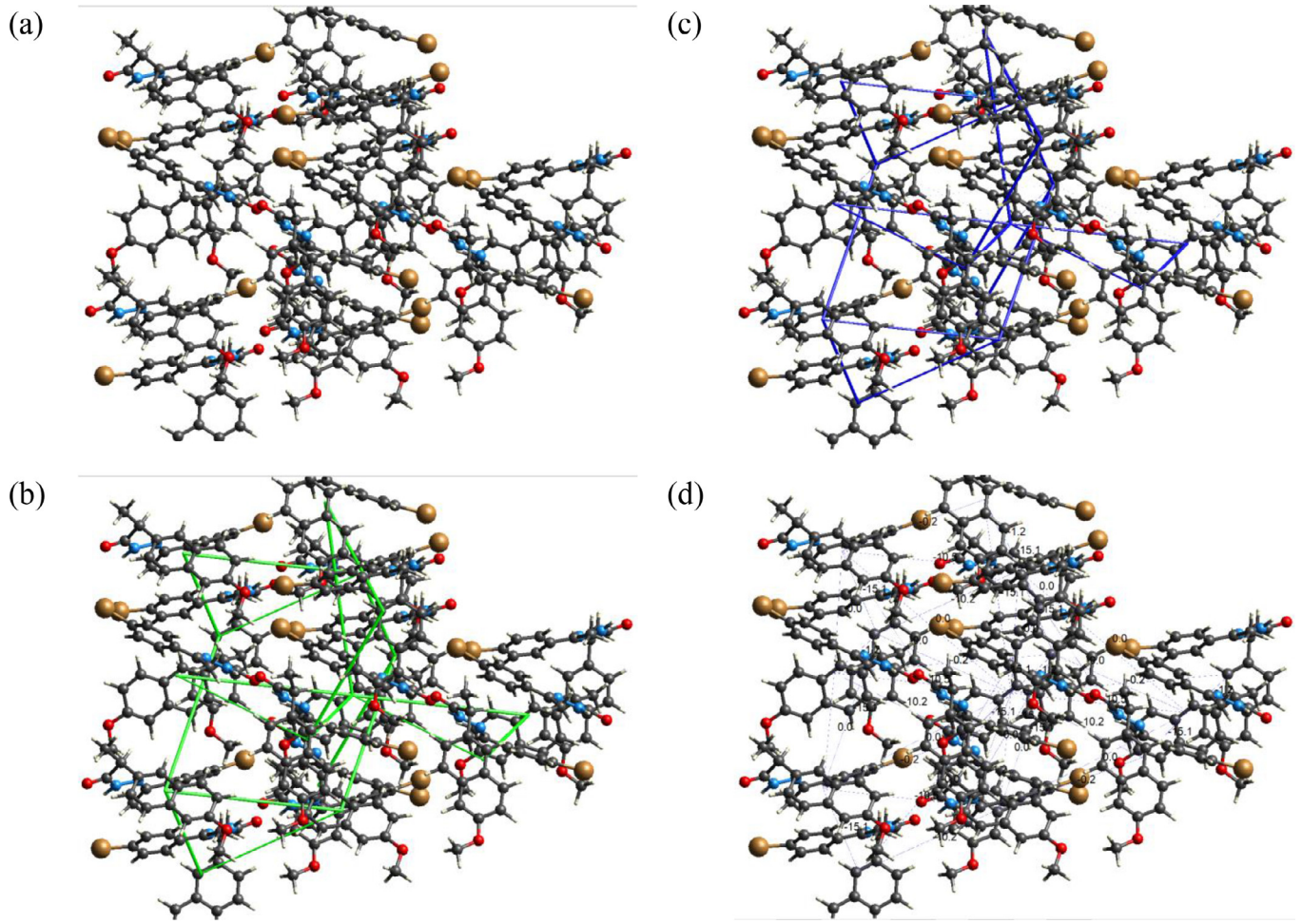

Fig. 6. The energy framework of the title compound (a) Coulomb energy, (b) dispersion energy, (c) total energy, and (d) total energy (annotated). tube size: 60, and cutoff: 5.00 kJ/mol).

The important aspect of the frontier molecular orbital theory is the focus on the highest occupied and lowest unoccupied molecular orbitals (HOMO and LUMO). Instead of thinking about the total electron density as a nucleophile, the localization of the HOMO orbital should be considered because electrons from this orbital have the most chance to participate in the nucleophilic attack, while a site where the lowest unoccupied orbital is localized is a good electrophilic site. The frontier molecular orbitals of the title compounds were further investigated in this study. As depicted in Fig. 8, there is a significant charge transfer if the transition from HOMO to LUMO occurs.

Molecular electrostatic potentials (MEPs) are fundamental measures of the interaction strength of the nearby charges, nuclei, and electrons at a particular position and thus enabling us to visualize the charge distribution and charge-related characteristics of molecules. To make data of the electrostatic potential easy to interpret, a visual representation with a chromatogram is used. Generally, red represents the lowest electrostatic potential value and may be attacked by electrophiles. On the contrary, blue represents the highest electrostatic potential value and may be attacked by nucleophiles. The full density matrix is used to generate the total density of the title compound and the resulting MEP is mapped on its surface. As depicted in Fig. 9, the oxygen atoms in the title compound are responsible for the nucleophilic attack because they have larger electronegativities than the other elements in the studied compound.

3.5. The result of the NBO analysis

The relative strength of the hydrogen bonds in the studied compounds could also be investigated by the second-order perturbation theory. As a hydrogen bond forms, there should be an orbital interaction between the nonbonding orbital of the hydrogen-bonded acceptor (n_A) and the antibonding orbital of the H-Donor bond ($\sigma_{H\text{-}D}{}^*$). The bond strength or bond order of the H-D bond should be thus weakened (decreased) due to such orbital interaction. In our previous study, the aforementioned orbital interaction was utilized to investigate the strongest hydrogen bond among several heterocyclic rings [56–58]. In this study, the correlation between the orbital interaction of n_A with $\sigma_{H\text{-}D}{}^*$ and the strength of a hydrogen bond is investigated to see whether or not such orbital interaction is a useful indicator for hydrogen bonds. Therefore, the interaction between a lone pair and the X-H antibonding orbital is summarized in Table 5. It is noteworthy that the interactions with interaction energy larger than 10 kcal/mol are listed in Table 5. The detailed NBO results about the interaction between a nonbonding orbital and an antibonding orbital are provided as the supporting information. As expected, the bromine and oxygen atom has three and two lone pairs, respectively. In this study, the three lone pairs of Br are symbolized as LP, LP' and LP". Similarly, the two lone pairs of O are symbolized as LP, and LP'. Interestingly, the lone pair on nitrogen doesn't show an orbital interaction with an interaction strength larger than 10 kcal/mol no matter with N4

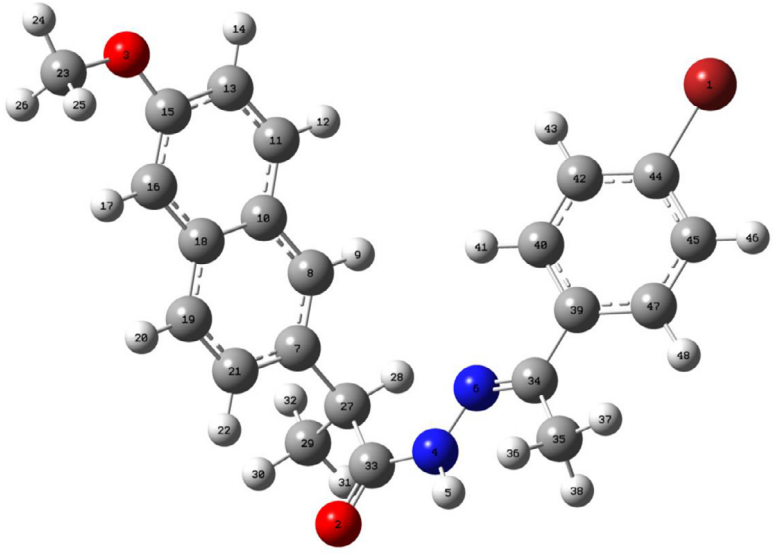

Fig. 7. The B3LYP-optimized geometry of the title compound (bond lengths in Å).

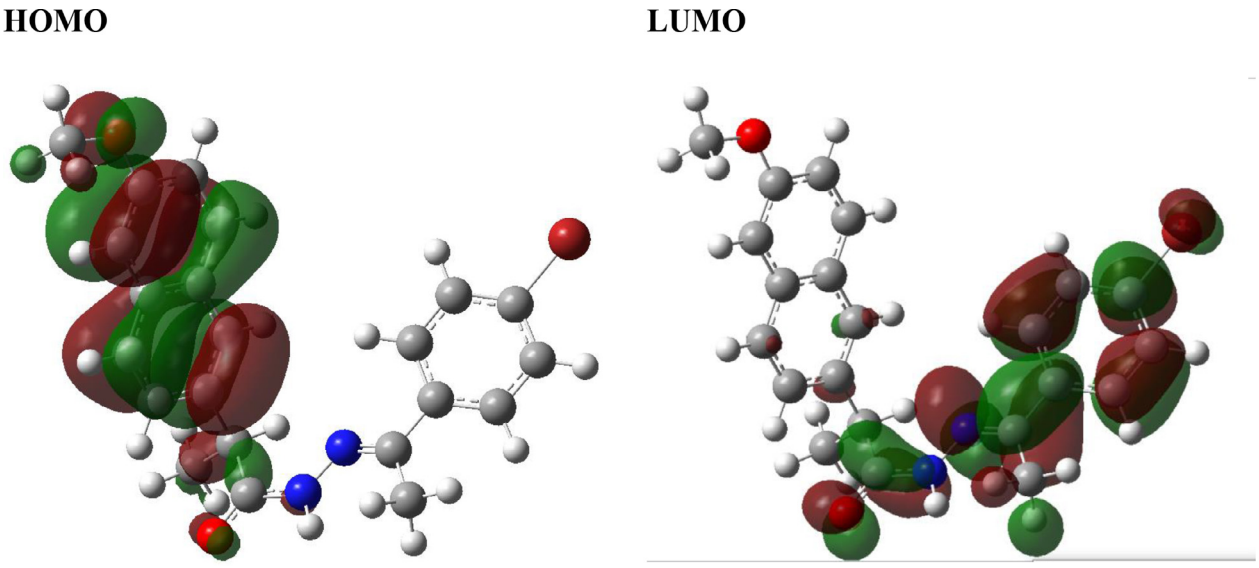

Fig. 8. The HOMO and LUMO of the studied compound (the isovalue= 0.02 a.u.).

Table 5
The NBO results of the title compound.

The type of n_A	The electron configuration of n_A	The type of orbital interaction	The interaction energy (in kcal/mol)[b]	The occupancy of $\sigma_{H\text{-}X}^*$	The bond order of $\sigma_{H\text{-}X}$[c]
LP(O2)[a]	s(58.95%)p(41.04%)d(0.02%)	LP(O2) -σ^*(C45-H46)[a]	21.56	0.01405	0.7943
LP''(Br1)[a]	s(0.00%)p(99.98%)d(0.02%)	LP''(Br1) -σ^*(C45-H46)[a]	20.96	0.01405	0.7943
LP'(O3)[a]	s(0.00%)p(99.96%)d(0.04%)	LP'(O3) -σ^*(C45-H46)[a]	19.17	0.01405	0.7943

[a] Please see the atomic designations in Fig. 7.
[b] The interaction energy was calculated based on the second-order perturbation theory.
[c] The listed values were the atom-atom overlap-weighted NAO bond order.

and N6 (please see the atomic designation in Fig. 7). Concerning the same antibonding orbital, σ^*(C45-H46), the lone pair on N4 and N6 show an interaction strength of 1.59 kcal/mol and 1.98 kcal/mol, respectively. As listed in Table 5, the strongest interaction among the whole molecule is an interaction between a lone pair of oxygen and an antibonding C-H orbital. However, from a distant perspective, both O2 and O3 have a long distance and should not form a hydrogen bond with the C45-H46 bond. The NBO analysis examines all possible interactions between filled Lewis-type NBOs and empty non-Lewis NBOs in the idealized Lewis structure. It estimates their interaction energies by the second-order perturbation theory. Since these interactions will cause the decrease in the oc-

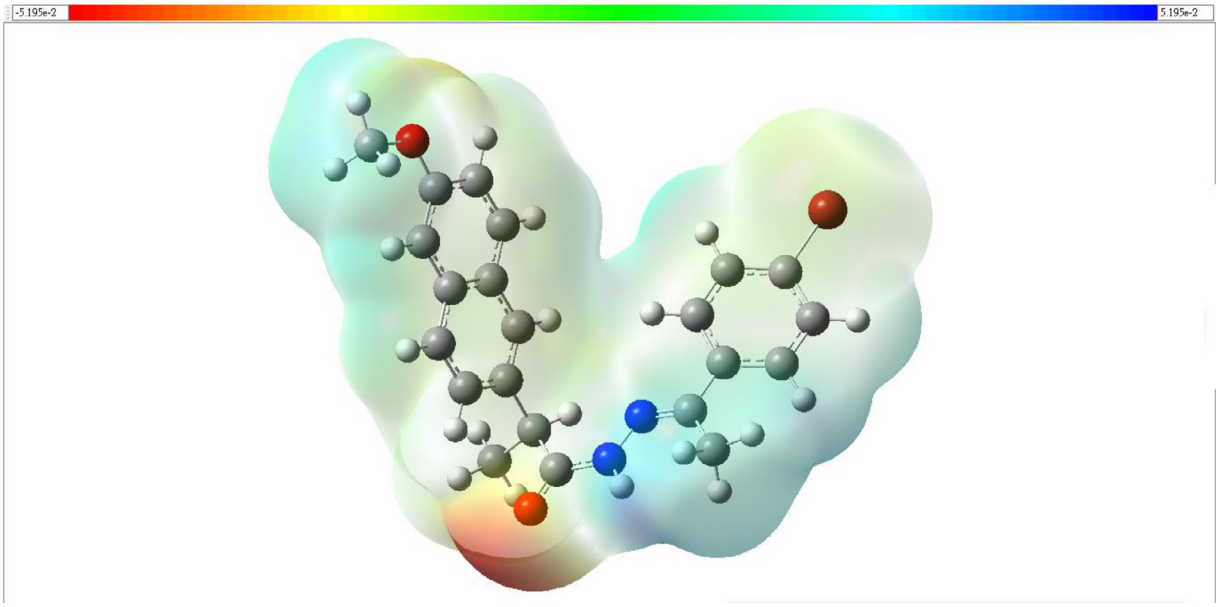

Fig. 9. The MEP of the studied compound (the isovalue= 0.0004 a.u).

cupancy of the filled NBOs and the increase in the occupancy of the empty non-Lewis orbitals, it thus makes the studied compound shows a departure from the idealized Lewis structure description. The resulting structure should be referred to as a delocalization correction to the zeroth-order natural Lewis structure. Accordingly, if one considers both the strength of the interaction between the n_A and $\sigma_{H\text{-}D}{}^*$ orbitals and the distance of the two orbitals, there should be a C-H···Br hydrogen bond in the title compound.

3.6. The QTAIM study

Under the condition that the Poincare-Hopf relationship is satisfied, the calculated BCP has a total of 105. There are 48, 52, 5, and 0 for the (3,-3), (3,-1), (3,+1), (3,+3) BCP, respectively. As depicted in Fig. 10, the (3,-3) BCP corresponds to the atomic nuclei. Except for the BCP numbered 63 and 81, the remaining (3,-1) BCPs correspond to the midpoint of the bond between the two nuclei. The (3,+1) BCPs numbered 75, 84, and 93 are the center of the three aromatic rings. However, the BCPs numbered 63, 65, and 81 are not between a hydrogen atom and a hydrogen-bonded acceptor. The electron density and the Laplacian of electron density of the (3,+1) BCP named 77 are 0.002 a.u. and 0.007 a.u., respectively. According to the aforementioned criteria about hydrogen bonding, the BCP designated as 77 should not indicate that there is an intramolecular hydrogen bond in the title compound. Although the NBO analysis and QTAIM study have already been used as powerful tools to investigate intra- or intermolecular hydrogen bonding of several systems [54,59–63], they seemed not to be suitable to describe the intramolecular hydrogen bonds among the title compound in this study.

3.7. Molecular docking

In this phase, the first molecular docking study was conducted to determine compound binding with the main protease enzyme. The binding affinity of the compound for the enzyme is -8.1 kcal/mol, in contrast, to control with a binding energy of -10.21 kcal/mol. The compound interacts with the active pocket of the enzyme and interacts with several key residues (Fig. 10). The 2-methoxynaphthalene of the compound was the major contributing chemical moiety responsible for hydrogen bonding with His31 and Cys145. Both these residues are critical in substrate binding and blocking both these are curtail from a drug design point of view. The (*E*)-1-((1-(4-bromophenyl)vinyl)diazenyl)prop-2-en-1-one is mainly involved in hydrophobic interactions with residues: Met49, Asn142, His164, Met165, Glu166, Leu167, Arg188, Gln189, and Thr190.

3.8. Molecular dynamics simulation

The structural dynamics stability of the complex was evaluated using a molecular dynamics simulation study. The analysis was run in duplicates to make sure accuracy of the results as shown in Fig. 11. The first statistical test performed on the complex trajectories is the root mean square deviation to superimpose all simulation frames on the docked complex. As can be seen in Fig. 11A, the system remained quite stable during simulation time with no major structural fluctuation noted. The run_1 and run _2 simulations complete each other very well and demonstrate the overall good stability of the complex. The mean RMSD in Run_1 is 1.6 Å while that in Run_2 is 1.56 Å. Next, a root means square fluctuation (RMSF) analysis was undertaken (Fig. 11B). A similar trend as that of RMSD was noticed. Despite few fluctuations at the N and C-terminal, most of the residues of the enzyme in particular active pocket residues are quite stable and enjoy the presence of a compound at the substrate-binding site. The mean RMSF of Run_1 is 1.3 Å while that for Run_2, it is 1.25 Å. Fig. 12

3.9. Binding free energy (MM-GBSA) calculations

MMPB\GBSA binding free energies were also estimated for the complex. The net binding energy for the complex predicted by MMGBSA is -37.41 kcal/mol while in MMPBSA the net binding energy of the complex is -40.5 kcal/mol. Both the methods revealed the formation of strong interactions between the enzyme and compound. In particular, the van der Waals energy is dominating overall binding energy in both methods, followed by a favorable contribution from electrostatic energy. The polar solvation energy is less contributes to the complex formation while non-polar solvation energy positively. The different binding energies of the complex are tabulated in Table 6.

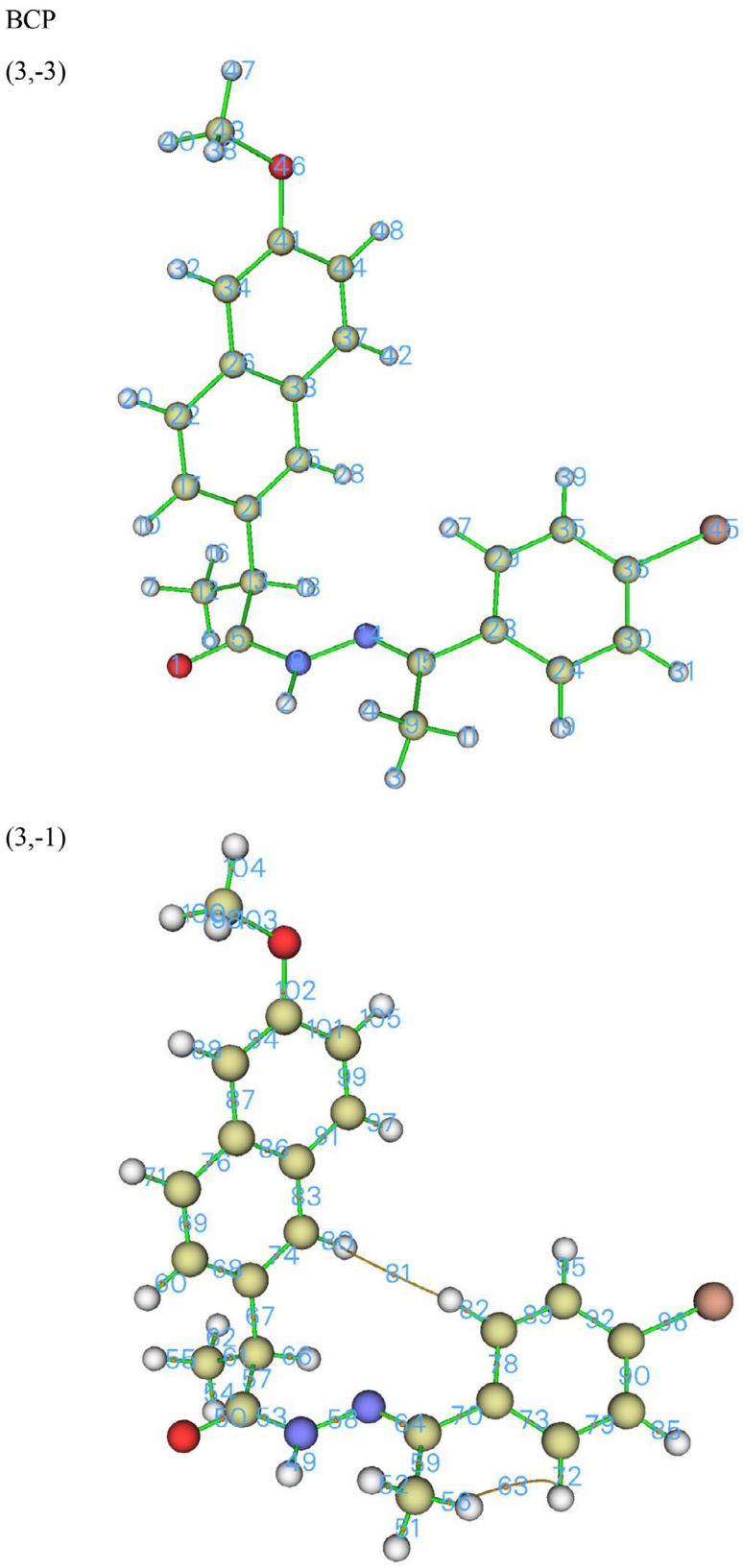

Fig. 10. The (3,-3), (3,-1), and (3,+1) BCPs of the title compound.

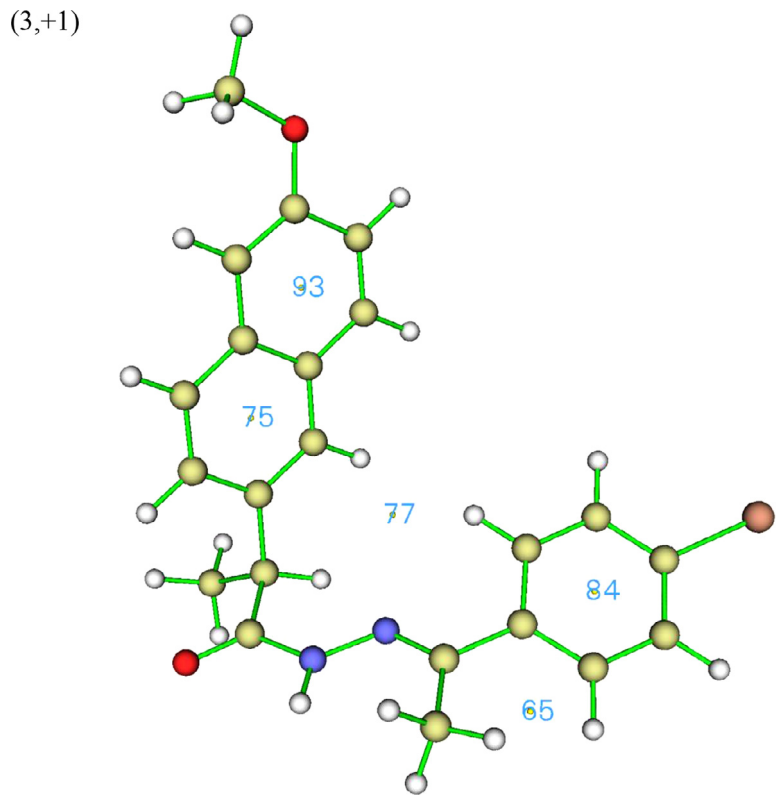

Fig. 10. Continued

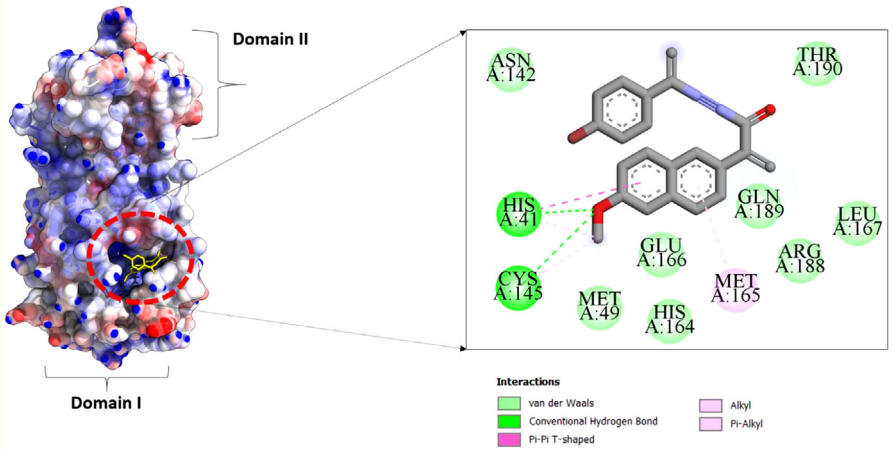

Fig. 11. Molecular docking of the compound with SARS-CoV-2 main protease and intermolecular binding interactions.

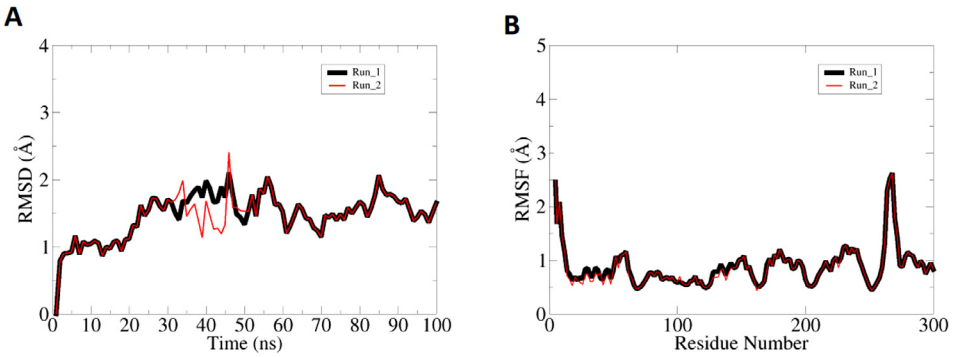

Fig. 12. Molecular dynamics simulation of the complex. A. RMSD and B. RMSF.

Table 6
Binding energies result in the complex. The values are reported in kcal/mol.

Energy Parameter	Value
MMGBSA	
Van der Waals Energy	-32.41
Electrostatic Energy	-20.38
Polar Solvation Energy	28.77
Non-polar Solvation Energy	-13.39
Delta Gas-Phase Energy	-52.79
Delta Solvation Energy	15.38
Delta Total	-37.41
MMPBSA	
Van der Waals Energy	-32.41
Electrostatic Energy	-20.38
Polar Solvation Energy	23.39
Non-polar Solvation Energy	-11.10
Delta Gas-Phase Energy	-52.79
Delta Solvation Energy	12.29
Delta Total	-40.5

4. Conclusion

Computer-aided drug design methods like molecular docking, molecular dynamics simulation, and binding free energy methods were used that predicted the compound strong binding with the SARS-CoV-2 main protease enzyme. The results found the compounds might serve as a good lead for future structure optimization. To obtain a structure-activity relationship, the DFT optimization and NBO analysis were thus performed to study the intrinsic electronic properties of the title compound. Although the MEP of the title compound derived from the gas-phase DFT optimization showed that the oxygen atom of the carbonyl group in the title compound should be the most negative site among the whole molecule, the result of the docking study showed that the oxygen atom of the carbonyl group in the title compound doesn't involve its binding concerning the SARS-CoV-2 main protease enzyme. This can be rationalized by the fact that the electrostatic interaction is not the major factor in the interaction between the title compound and the other molecule. Based on the result of the free energy calculation, the major factor in its interaction with the SARS-CoV-2 main protease enzyme is the van der Waals interaction. In agreement with the result of the free energy calculation, the energy framework showed the interaction between the title compound and the other molecules is mainly contributed by the dispersion interaction. Based on the energy framework analysis, the term E_dis is the most important contributor to E_tot although the central molecule forms hydrogen bonds with its neighboring molecules; which is similar to the previous studies about the related nitrogenated species. Although the NBO analysis and QTAIM study have already been used as powerful tools to investigate intra- or intermolecular hydrogen bonding of several systems, they seemed not to be suitable to describe the intramolecular hydrogen bonds among the title compound in this study. Moreover, the Hirshfeld surface analysis shows that the $\pi\cdots\pi$ stacking does not play an important role in the crystal packing of the title compound; which is also similar to the related nitrogenated species in the previous studies.

CRediT authorship contribution statement

Dalia A. Abdul: Synthesized and characterized the title molecule. **Youness El Bakri:** Data curation, Wrote the paper; Final approval of the version submitted. **Sajjad Ahmad and Chin-Hung Lai:** Writing-reviewing and performed quatum-chemical calculations, analyzed and interpreted the data. **Mustafa R Albayati:** Visualization, Invistigation and data curation. **Joel T. Mague:** Performed the X-ray experiments and analyzed and interpreted the data. **Shaaban K. Mohamed and Mahmoud S. Tolba:** Conceptualization and supervision.

Declaration of Competing Interest

Authors declare that there is no competing interest

Supplementary materials

Supplementary material associated with this article can be found, in the online version, at doi:10.1016/j.molstruc.2022.133391.

References

[1] M.S. Tolba, A.M. Ked, M. Ahmed, R. Hassanien, M. Sayed, R.M. Zaki, S.K. Mohamed, S.A. Zawam, A.A. Ars, Synthesis, reactions, and applications of pyrimidine derivatives, Curr. Chem. Lett. (2021).
[2] S.A.A. Abdel-Raheem, A.M.K. El-Dean, R. Hassanien, M.E.A. El-Sayed, A.A. Abd-Ella, Synthesis and characterization of some distyryl derivatives for agricultural uses, Eur. Chem. Bull. 10 (2021) 35–38.
[3] M.S. Tolba, M.A. Abd ul-Malik, A.M. Kamal El-Dean, A.A. Geies, M. Radwan Sh, R.M. Zaki, M. Sayed, S.K. Mohamed, A.A. Abdel-Raheem Sh, An overview on synthesis and reactions of coumarin based compounds, Curr. Chem. Lett. (2021).
[4] O. Terrier, S. Dilly, A. Pizzorno, D. Chalupska, J. Humpolickova, E. Bouřa, F. Berenbaum, S. Quideau, B. Lina, B. Fève, Antiviral Properties of the NSAID Drug Naproxen Targeting the Nucleoprotein of SARS-CoV-2 Coronavirus, Molecules 26 (2021) 2593.
[5] Y.A. Ammar, M.A. Salem, E.A. Fayed, M.H. Helal, M.S.A. El-Gaby, H.K. Thabet, Naproxen derivatives: synthesis, reactions, and biological applications, Synth. Commun 47 (2017) 1341–1367.
[6] M.R. Rodrigues, C.M. Lanzarini, E. Ricci-Junior, Preparation, in vitro characterization and in vivo release of naproxen loaded in poly-caprolactone nanoparticles, Pharm. Dev. Technol. 16 (2011) 12–21.
[7] M.H. Helal, S.Y. Abbas, M.A. Salem, A.A. Farag, Y.A. Ammar, Synthesis and characterization of new types of 2-(6-methoxy-2-naphthyl) propionamide derivatives as potential antibacterial and antifungal agents, Med. Chem. Res. 22 (2013) 5598–5609.
[8] Y.X. Wang, J. Zhao, X.Q. Sun, C.J. Wang, Synthesis, interaction with DNA and bioactivity of N-piperazinoalkylamide, CHINESE J. Org. Chem. 26 (2006) 1066–1072.
[9] A. Rigg, B. Russell, M. Van Hemelrijck, C. Moss, COVID-19 and treatment with NSAIDs and corticosteroids: should we be limiting their use in the clinical setting?, (2020).
[10] P. Little, Non-steroidal anti-inflammatory drugs and covid-19, (2020).
[11] E.G. Favalli, F. Ingegnoli, O. De Lucia, G. Cincinelli, R. Cimaz, R. Caporali, COVID-19 infection and rheumatoid arthritis: Faraway, so close!, Autoimmun. Rev. 19 (2020) 102523.
[12] J.V. Pergolizzi, G. Varrassi, P. Magnusson, J.A. LeQuang, A. Paladini, R. Taylor, C. Wollmuth, F. Breve, P. Christo, COVID-19, and NSAIDS: a narrative review of knowns and unknowns, Pain Ther. 9 (2020) 353–358.
[13] M.T. Kelleni, Early use of non-steroidal anti-inflammatory drugs in COVID-19 might reverse pathogenesis, prevent complications and improve clinical outcomes, Biomed. Pharmacother. 133 (2021) 110982.
[14] W. Zheng, W. Fan, S. Zhang, P. Jiao, Y. Shang, L. Cui, M. Mahesutihan, J. Li, D. Wang, G.F. Gao, Naproxen exhibits broad anti-influenza virus activity in mice by impeding viral nucleoprotein nuclear export, Cell Rep 27 (2019) 1875–1885.
[15] C. Amici, A. Di Caro, A. Ciucci, L. Chiappa, C. Castilletti, V. Martella, N. Decaro, C. Buonavoglia, M.R. Capobianchi, M.G. Santoro, Indomethacin has a potent antiviral activity against SARS coronavirus, Antivir. Ther. 11 (2006) 1021.
[16] N. Lejal, B. Tarus, E. Bouguyon, S. Chenavas, N. Bertho, B. Delmas, R.W.H. Ruigrok, C. Di Primo, A. Slama-Schwok, Structure-based discovery of the novel antiviral properties of naproxen against the nucleoprotein of influenza A virus, Antimicrob. Agents Chemother. 57 (2013) 2231–2242.
[17] I. Kickbusch, G. Leung, Response to the emerging novel coronavirus outbreak, (2020).
[18] G. O'Mara, Could ACE inhibitors and particularly ARBs increase susceptibility to COVID-19 infection, BMJ 368 (2020) m406.
[19] G.A. FitzGerald, Misguided drug advice for COVID-19, Science 367 (2020) 1434 (80).
[20] G. Voiriot, Q. Philippot, A. Elabbadi, C. Elbim, M. Chalumeau, M. Fartoukh, Risks related to the use of non-steroidal anti-inflammatory drugs in community-acquired pneumonia in adult and pediatric patients, J. Clin. Med. 8 (2019) 786.
[21] M. Le Bourgeois, A. Ferroni, M. Leruez-Ville, E. Varon, C. Thumerelle, F. Brémont, M.J. Fayon, C. Delacourt, C. Ligier, L. Watier, Children, Antibiotics, Non-steroidal Anti-inflammatory Drugs and Childhood Empyema (ChANCE) Study Group. Nonsteroidal anti-inflammatory drug without antibiotics for acute viral infection increases the empyema risk in children: a matched case-control study, J Pediatr 175 (2016) 47–53.

[22] N. Bhala, J. Emberson, A. Merhi, S. Abramson, N. Arber, J.A. Baron, C. Bombardier, C. Cannon, M.E. Farkouh, G.A. FitzGerald, Coxib and traditional NSAID Trialists'(CNT) Collaboration. Vascular and upper gastrointestinal effects of non-steroidal anti-inflammatory drugs: meta-analyses of individual participant data from randomised trials, Lancet 382 (2013) 769–779.
[23] H. Baradaran, H. Hamishehkar, H. Rezae, NSAIDs and COVID-19: A new challenging area, Pharm. Sci. 26 (2020) S49–S51.
[24] SAINT. Data Reduction and Correction Program.Version 8.34A. Bruker AXS Inc., Madison, Wisconsin, USA, 2014, (n.d.).
[25] L. Krause, R. Herbst-Irmer, G.M. Sheldrick, D. Stalke, Comparison of silver and molybdenum microfocus X-ray sources for single-crystal structure determination, J. Appl. Crystallogr. 48 (2015) 3–10.
[26] G.M. Sheldrick, SHELXT - Integrated space-group and crystal-structure determination, Acta Crystallogr. Sect. A Found. Crystallogr. 71 (2015) 3–8, doi:10.1107/S2053273314026370.
[27] G.M. Sheldrick, Crystal structure refinement with SHELXL, Acta Crystallogr. Sect. C Struct. Chem. 71 (2015) 3–8, doi:10.1107/S2053229614024218.
[28] M.A. Spackman, P.G. Byrom, A novel definition of a molecule in a crystal, Chem. Phys. Lett. 267 (1997) 215–220.
[29] J.J. McKinnon, M.A. Spackman, A.S. Mitchell, Novel tools for visualizing and exploring intermolecular interactions in molecular crystals, Acta Crystallogr. Sect. B Struct. Sci. 60 (2004) 627–668.
[30] M.A. Spackman, D. Jayatilaka, Hirshfeld surface analysis, CrystEngComm 11 (2009) 19–32.
[31] C.F. Mackenzie, P.R. Spackman, D. Jayatilaka, M.A. Spackman, CrystalExplorer model energies and energy frameworks: extension to metal coordination compounds, organic salts, solvates and open-shell systems, IUCrJ 4 (2017) 575–587.
[32] M.J. Turner, J.J. McKinnon, S.K. Wolff, D.J. Grimwood, P.R. Spackman, D. Jayatilaka, M.A. Spackman, CrystalExplorer, 17, (2017).
[33] A.D. Beck, Density-functional thermochemistry. III. The role of exact exchange, J. Chem. Phys. 98 (1993) 5646–5648.
[34] C. Lee, W. Yang, R.G. Parr, Development of the Colle-Salvetti correlation-energy formula into a functional of the electron density, Phys. Rev. B. 37 (1988) 785.
[35] B. Miehlich, A. Savin, H. Stoll, H. Preuss, Results obtained with the correlation energy density functionals of Becke and Lee, Yang and Parr, Chem. Phys. Lett. 157 (1989) 200–206.
[36] A.D. McLean, G.S. Chandler, Contracted Gaussian basis sets for molecular calculations. I. Second row atoms, Z=11-18, J. Chem. Phys. 72 (1980) 5639–5648, doi:10.1063/1.438980.
[37] M.J. Frisch, G.W. Trucks, H.B. Schlegel, G.E. Scuseria, M.A. Robb, J.R. Cheeseman, G. Scalmani, V. Barone, G.A. Petersson, H. Nakatsuji, Gaussian 16, (2016).
[38] T. Lu, F. Chen, Multiwfn: A Multifunctional Wavefunction Analyzer, J. Comput.Chem 33 (2002) 580–592, doi:10.1002/jcc.22885.
[39] U. Koch, P.L.A. Popelier, Characterization of C-H-O Hydrogen Bonds on the Basis of the Charge Density, J. Phys. Chem. 99 (1995) 9747–9754, doi:10.1021/j100024a016.
[40] G.M. Morris, M. Lim-Wilby, Molecular docking, in: Mol Model Proteins, Springer, 2008, pp. 365–382.
[41] E.F. Pettersen, T.D. Goddard, C.C. Huang, G.S. Couch, D.M. Greenblatt, E.C. Meng, T.E. Ferrin, UCSF Chimera a visualization system for exploratory research and analysis, J. Comput. Chem. 25 (2004) 1605–1612.
[42] K.R. Cousins, Computer review of ChemDraw ultra 12.0, (2011).
[43] R. Huey, G.M. Morris, Using AutoDock 4 with AutoDocktools: a tutorial, Scripps Res. Institute, USA. (2008) 54–56.
[44] D. Studio, Discovery Studio, Accelrys [2.1]. (2008).
[45] D.A. Case, H.M. Aktulga, K. Belfon, I.Y. Ben-Shalom, S.R. Brozell, D.S. Cerutti, T.E. Cheatham III, G.A. Cisneros, V.W.D. Cruzeiro, T.A. Darden, Amber 2021, University of California Press, 2021.
[46] U. Essmann, L. Perera, M.L. Berkowitz, T. Darden, H. Lee, L.G. Pedersen, A smooth particle mesh Ewald method, J. Chem. Phys. 103 (1995) 8577–8593.
[47] V. Kräutler, W.F. Van Gunsteren, P.H. Hünenberger, A fast SHAKE algorithm to solve distance constraint equations for small molecules in molecular dynamics simulations, J. Comput. Chem. 22 (2001) 501–508.
[48] D.R. Roe, T.E. Cheatham III, PTRAJ and CPPTRAJ: software for processing and analysis of molecular dynamics trajectory data, J. Chem. Theory Comput. 9 (2013) 3084–3095.
[49] P. Turner, XMGRACE, Version 5.1. 19. Cent Coast Land-Margin Res Oregon Grad Inst Sci Technol Beavert, (2005).
[50] B.R. Miller, T.D. McGee, J.M. Swails, N. Homeyer, H. Gohlke, A.E. Roitberg, MMPBSA.py: An efficient program for end-state free energy calculations, J. Chem. Theory Comput. 8 (2012) 3314–3321, doi:10.1021/ct300418h.
[51] S. Genheden, U. Ryde, The MM/PBSA and MM/GBSA methods to estimate ligand-binding affinities, Expert Opin. Drug Discov. 10 (2015) 449–461, doi:10.1517/17460441.2015.1032936.
[52] A. Saeed, S. Ashraf, U. Flörke, Z.Y.D. Espinoza, M.F. Erben, H. Pérez, Supramolecular self-assembly of a coumarine-based acylthiourea synthon directed by π-stacking interactions: Crystal structure and Hirshfeld surface analysis, J. Mol. Struct. 1111 (2016) 76–83.
[53] A. Saeed, U. Flörke, A. Fantoni, A. Khurshid, H. Pérez, M.F. Erben, Close insight into the nature of intermolecular interactions in dihydropyrimidine-2 (1h)-thione derivatives, CrystEngComm 19 (2017) 1495–1508.
[54] A. Saeed, M. Bolte, M.F. Erben, H. Pérez, Intermolecular interactions in crystalline 1-(adamantane-1-carbonyl)-3-substituted thioureas with Hirshfeld surface analysis, CrystEngComm 17 (2015) 7551–7563.
[55] A. Saeed, A. Khurshid, U. Flörke, G.A. Echeverría, O.E. Piro, D.M. Gil, M. Rocha, A. Frontera, H.R. El-Seedi, A. Mumtaz, Intermolecular interactions in antipyrine-like derivatives 2-halo-N-(1, 5-dimethyl-3-oxo-2-phenyl-2, 3-dihydro-1 H-pyrazol-4-yl) benzamides: X-ray structure, Hirshfeld surface analysis and DFT calculations, New J. Chem. 44 (2020) 19541–19554.
[56] W. Al Garadi, Y. El Bakri, C.H. Lai, L. El Ghayati, J.T. Mague, E.M. Essassi, Synthesis, X-ray, spectroscopic characterization, Hirshfeld surface analysis, DFT calculation and molecular docking investigations of a novel 7-phenyl-2, 3, 4, 5-tetrahydro-1H-1, 4-diazepin-5-one derivative, J. Mol. Struct. 1234 (2021) 130146.
[57] Y. El Bakri, C.H. Lai, S. Karthikeyan, L. Guo, S. Ahmad, A. Ben-Yahya, J.T. Mague, E.M. Essassi, Synthesis, Crystal structure, Hirshfeld surface Analysis and computational approach of new 2-methylbenzimidazo [1, 2-a] pyrimidin-4 (1H)-one, J. Mol. Struct. 1239 (2021) 130497.
[58] L.H. Abdel-Rahman, S.K. Mohamed, Y. El Bakri, S. Ahmad, C.-H. Lai, A.A. Amer, J.T. Mague, E.M. Abdalla, Synthesis, crystal structural determination and in silco biological studies of 3, 3′-ethane-1, 2-diylbis (2-benzylidene-1, 3-thiazolidin-4-one, J. Mol. Struct. 1245 (2021) 130997.
[59] M. Xu, B. Zhang, Qi Wang, Y. Yuan, L. Sun, Z. Huang, Theoretical Study on The Hydrogen Bonding Interactions in Paracetamol-Water Complexes, J. Chil. Chem. Soc. 63 (2018) 3788–3794.
[60] M.J. Javan, Effect of multiple & cooperative intramolecular hydrogen bonding on polyhydroxylated thiopyrans acidities: Detailed view from AIM & NBO analyses, Comput. Theor. Chem. (2021) 113440 1205.
[61] M.K. Chaudhary, T. Karthick, B. DattJoshi, P. Prajapati, M.S.A. Santana, A.P. Ayala, V.S. Jeba Reeda, P. Tandon, Molecular structure and quantum descriptors of cefradine by using vibrational spectroscopy (IR and Raman), NBO, AIM, chemical reactivity and molecular docking, Spectrochim. Acta A 246 (2021) 118976.
[62] I.N. Kolesnikova, N.A. Chegodaev, P.Y. Sharanov, I.F. Shishkov, Equilibrium molecular structure and intramolecular interactions of picolinic acid hydrazide, Chem. Phys. Lett. 793 (2022) 139447.
[63] A. Jezierska, J.J. Panek, K. Błaziak, K. Raczyński, A. Koll, Exploring Intra- and Intermolecular Interactions in Selected N-Oxides—The Role of Hydrogen Bonds, Molecules 27 (2022) 792.